Photodetectors: UV to IR

Joe C. Campbell[a], Shuling Wang[a], Xiaoguang Zheng[a], Xioawei Li[a], Ning Li[a], Feng Ma[a], Xiaoguang Sun[a], Charles J. Collins[b], A. L. Beck[a], B. Yang[a], Jeffrey B. Hurst[a], Rubin Sidhu[a], Archie L. Holmes[a], Jr.[a], U. Chowdhury[a], Michael M. Wong[a], Russell D. Dupuis[a], Andrew Huntington[c], Larry A. Coldren[c], Zhonghui Chen[d], Eui-Tae Kim[d], and Anupam Madhukar[d]

[a]Microelectronics Research Center, The University of Texas, Austin, TX 78712

[b]Army Research Laboratory, Adelphi, MD 20783

[c]Optoelectronics Technology Center, University of California, Santa Barbara, CA 93106

[d]Dept. of Materials Science and Physics, University of Southern California, Los Angeles, CA 90089

ABSTRACT

This paper surveys recent work in several photodetector areas including high-speed, low-noise avalanche photodiodes, high-power photodiodes, solar-blind ultra-violet PIN photodiodes, and quantum dot infrared photodetectors (QDIPs).

Key words: avalanche photodiode, impact ionization, ultra-violet photodiode, quantum dot, infrared photodetector, photoresponse, detectivity

1. SOLAR-BLIND ULTRA-VIOLET PHOTODIODES

Recently the development of $Al_xGa_{1-x}N$ wide-bandgap semiconductor devices for ultraviolet (UV) photon detection has been the subject of intense research [1]. The advantages of this material system include wide-bandgap, chemical stability, high breakdown fields, and the potential for high-temperature device operation [2]. AlGaN photodetectors have potential applications in chemical sensing, flame detection, ozone-hole sensing, secure short-range communication, and missile plume sensing [3-6]. Strong atmospheric absorption of sunlight, in a narrow UV band from 240-290nm, creates a low background radiation regime at the Earth's surface. Recently, many photodetectors have been designed to operate in this wavelength range, which is referred to as the "solar-blind" region [7-10]. For array

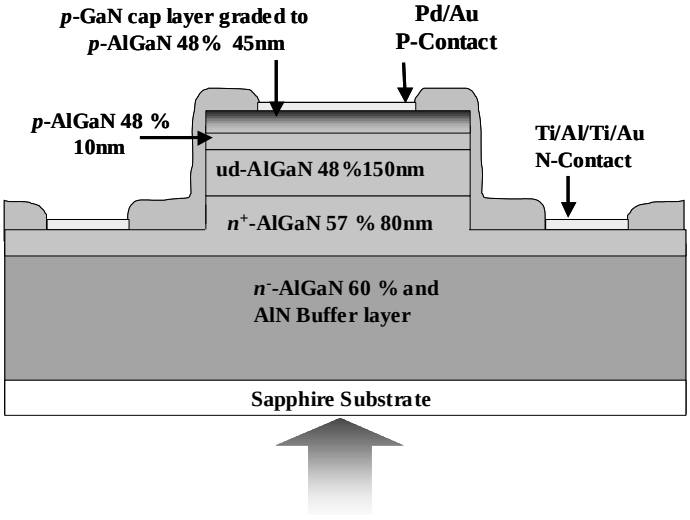

Figure 1. Schematic cross section of a $Al_xGa_{1-x}N$ solar-blind photodiode.

Active and Passive Optical Components for WDM Communications III, Achyut K. Dutta, Abdul Ahad S. Awwal, Niloy K. Dutta, Kazuo Fujiura, Proceedings of SPIE Vol. 5246 (2003)

applications, photodetectors are designed to be back-illuminated in order to facilitate flip-chip mounting of the arrays to silicon readout circuits [5,6]. Devices that work at the low biases of traditional silicon readout circuitry are desirable. In addition, a low operating voltage will allow one to take advantage of the large differential resistance near zero-bias leading to large detectivities.

A schematic of the solar-blind photodetector is shown in Fig. 1. Device layers for the p-i-n structure consists of an 80 nm-thick $Al_{0.60}Ga_{0.40}N$ n^+-layer, a 150 nm-thick $Al_{0.45}Ga_{0.55}N$ unintentionally doped ($N_d \approx 10^{15}$ cm^{-3}) absorption region, a 10 nm-thick $Al_{0.45}Ga_{0.55}N$ p-layer, whose function is to pin the depletion region and keep it from extending into the cap layer, a 20 nm-thick graded $Al_{0.45}Ga_{0.55}N$ to GaN p-layer, and a 25 nm-thick p-GaN contact layer. A GaN cap layer is used to improve the p-contact; the GaN/AlGaN heterojunction blocks photogenerated electrons in the cap layer from diffusing into the i-region [11].

The external quantum efficiency at different reverse bias voltages and the zero-bias responsivity is plotted in Fig. 2. The difference in the aluminum percentage of the n-layer and i-layer was kept as large as possible while still maintaining a solar-blind response. This aluminum percentage difference insures good transmission to the i-layer resulting in a spectral response with 20 nm FWHM. The peak zero-bias external quantum efficiency was ~53% at 275 nm which increased to ~58% at a reverse bias of 5V, corresponding to peak responsivities of 0.12 A/W and 0.13 A/W, respectively. The external quantum efficiency reached a plateau at a value of ~60% at a reverse bias of 10V. Figure 2 shows that by 300 nm the responsivity dropped by three orders of magnitude from its peak value. The long-wavelength response that was visible in previous devices is absent [12].

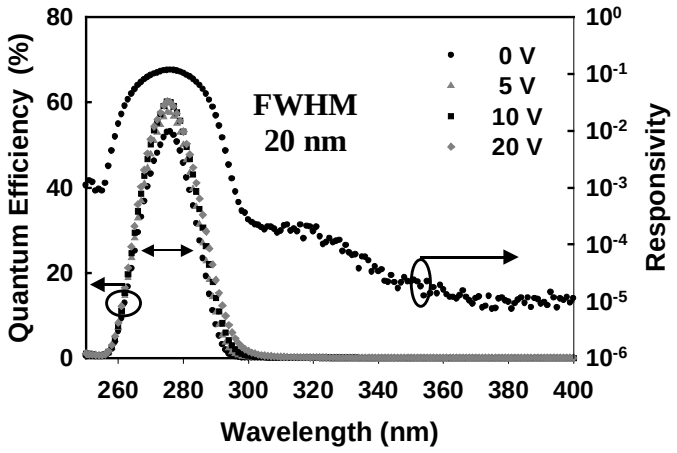

Figure 2. External quantum efficiency vs. wavelength for a solar-blind detector showing a 275 nm zero-bias peak of 53%. The right axis shows the corresponding zero-bias responsivity of 0.12 A/W at 275 nm.

The dark current density was 8.2×10^{-11} A/cm^2 at a reverse bias of 5V and increased only slightly to 1.5×10^{-9} A/cm^2 at 10V. When back-illuminated with a broadband UV light source, there was a strong, flat photoresponse. In forward bias, the current density was 17 A/cm^2 at 10V. The series resistance, $R_S = 360\ \Omega$, was estimated by plotting I(dV/dI) vs. I as described in Ref. [3]. We attribute the low forward resistance to good ohmic contacts and conductive p-type GaN, p-type $Al_{0.45}Ga_{0.55}N$, and n-type $Al_{0.6}Ga_{0.4}N$ layers. Since these devices operate in the solar-blind region where the background radiation is very low, it is assumed that thermal noise is dominant. For this case, the specific detectivity, D^*, can be calculated from the differential resistance R_O, the device area A, and the zero-bias responsivity R_λ[1,12,13]. The differential resistance R_O, is related to the dark current and increases as the dark current decreases [12]. In order to calculate the differential resistance, a previously described method of exponential curve fitting to the dark current was used [14]. The derivative of the fitted curve at zero-bias yielded a differential resistance of $R_O = 2.51\times10^{14}$ Ω. Using the device diameter of 250 μm, the value of R_OA was $1.23\times10^{11}\ \Omega\cdot cm^2$. These parameters yield a value of $D^* = 3.0\times10^{14}$ $cm\cdot Hz^{1/2}\cdot W^{-1}$ at $\lambda = 275$ nm. We note that this detectivity is comparable to the detectivity of the photocathode of a photomultiplier tube [1].

2. AVALANCHE PHOTODIODES

2.1 Long-wavelength, impact-ionization-engineered avalanche photodiodes

Avalanche photodiodes (APD) are frequently the photodetectors of choice in high-bit-rate, long-haul fiber optic communication systems due to their internal gain. APDs can achieve 5-10 dB higher sensitivity than

PINs, provided that the multiplication noise is low and the gain-bandwidth product of the APD is sufficiently high. In determining its gain, multiplication noise, and the gain-bandwidth product, the multiplication region of an APD plays a critical role. Sub-micron scaling [15-24] of the thickness of the multiplication region has been found to give lower multiplication noise and higher gain-bandwidth products in APDs. This is due to the non-local nature of impact ionization, which can be neglected if the thickness of the multiplication region is much greater than the "dead length", which is the minimum distance carriers travel to gain sufficient energy to impact ionize. We have demonstrated that Impact-Ionization-Engineering (I^2E) [25-28] of the multiplication region of an APD can achieve very low-noise by utilizing beneficially designed heterostructures. Monte Carlo simulation [29] has revealed spatial modulation of the carrier impact ionization process in the I^2E structures.

Owing to the relatively mature growth technology and the well-documented material characteristics of $Al_xGa_{1-x}As$, GaAs/$Al_xGa_{1-x}As$ heterojunctions were used to study the transport mechanisms in the I^2E structures in Ref. 25 to 28. Recently, we have extended this concept to operation at longer wavelengths by growth of I^2E structures using InAlAs and InGaAlAs in the multiplication regions. These structures were chosen based on the following: 1) they worked well in lowering the excess noise factor in the GaAs/AlGaAs material system, and 2) like AlGaAs, the InGaAlAs quaternary materials have a relatively wide range of band gap energies. Compared to homojunction InAlAs and InP APDs, lower excess noise and comparable dark current have been achieved. Figure 3 shows the device cross-sectional view for the InP-based I^2E APDs. Owing to the larger ionization coefficients of the electrons relative to holes, a p-"i"-n structure and top-illumination were adapted to ensure pure electron injection: the unintentionally doped multiplication region structure was sandwiched between p-type ($3x10^{18}$ cm^{-3}, 0.8 μm) and n-type ($5x10^{18}$ cm^{-3}, 0.5 μm) $In_{0.52}Al_{0.48}As$ layers, with a highly p-doped (>$5x10^{18}$ cm^{-3}, ~30 nm) $In_{0.53}Ga_{0.47}As$ contact layer.

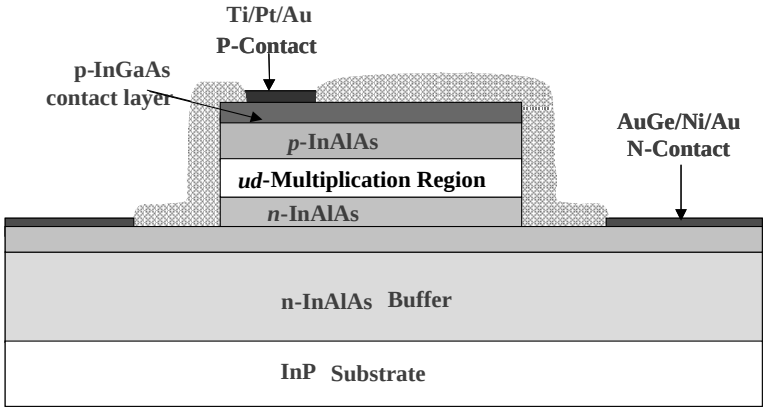

Figure 3. Schematic cross-section of the I^2E APD structure.

Shown in Fig. 4 are the two I^2E multiplication region structures designed on InP-substrates. A single-well

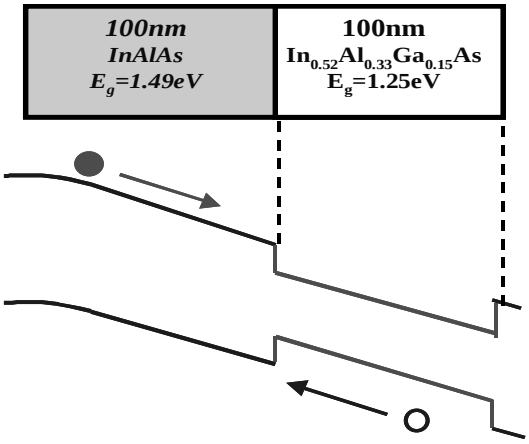

Figure 4(a). Schematics and energy band diagrams of the single-well structure.

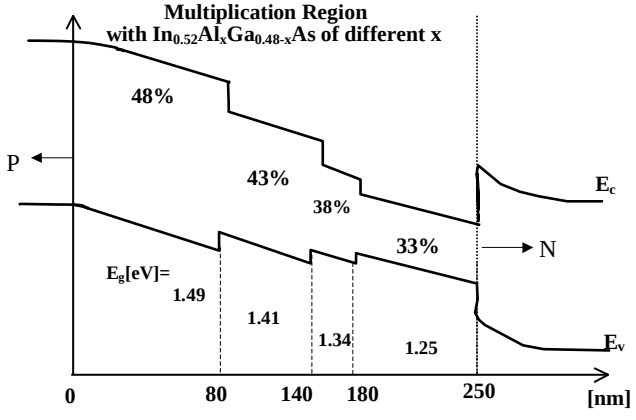

Figure 4(b). Schematics and energy band diagrams of the graded structure.

structure, as shown in Fig. 4(a), consisted of a 100nm-thick $In_{0.52}Al_{0.48}As$ layer at the p-side followed by a 100nm-thick $In_{0.52}Ga_{0.15}Al_{0.33}As$ quaternary layer. The lower band gap energy of $In_{0.52}Ga_{0.15}Al_{0.33}As$ (estimated to be ~1.25 eV [30]) as compared to $In_{0.52}Al_{0.48}As$ results in a lower carrier ionization threshold energy (E_{th}). There are relatively few ionization events in the $In_{0.52}Al_{0.48}As$ layer, owing to the combined effects of "dead space" [31] and the higher threshold energy in $In_{0.52}Al_{0.48}As$. Once the electrons reach the $In_{0.52}Ga_{0.15}Al_{0.33}As$ layer, they tend to ionize quickly because it has a lower threshold energy and the electrons have gained energy in the $In_{0.52}Al_{0.48}As$ portion of the multiplication region [28]. The secondary hole ionization rate also peaks in the $In_{0.52}Ga_{0.15}Al_{0.33}As$ well. However, after these secondary holes lose energy through impact ionization in the well region, their ionization probability is low in the $In_{0.52}Al_{0.48}As$ region due to its higher hole-ionization threshold energy. This significantly reduced the number of secondary hole ionization events. Therefore, in this single-well structure, both electron and hole ionization are expected to be localized in the $In_{0.52}Ga_{0.15}Al_{0.33}As$ well, while the ionization of both carrier types are suppressed in the $In_{0.52}Al_{0.48}As$ layer. The increased localization of the multiplication process relative to homojunction APDs is the origin of the low excess noise characteristics.

The structure shown in Fig. 4(b) was implemented on an InP-substrate using lattice-matched InAlGaAs quaternary materials as the multiplication region, based on a similar structure in $Al_xGa_{1-x}As/GaAs$ that was reported in Ref. [27]. Utilizing the decreasing band gap energies (thus decreasing ionization threshold energies) in $In_{0.52}Ga_{0.48-y}Al_yAs$ with decreasing Al content [30], the structure consisted of an 80-nm $In_{0.52}Al_{0.48}As$ layer followed by layers of 60-nm $In_{0.52}Ga_{0.05}Al_{0.43}As$, 40-nm $In_{0.52}Ga_{0.10}Al_{0.38}As$, and 70-nm $In_{0.52}Ga_{0.15}Al_{0.33}As$. The "graded" layer thickness were selected to decrease with decreasing bandgap energy because the dead space decreases with E_g. As discussed in detail in Ref. [27], the ionization events for electrons are expected to localize in the low-E_{th} layers, while the ionization of the secondary holes can be suppressed because the holes enter materials with increasing ionization threshold energies as they travel toward the p-region.

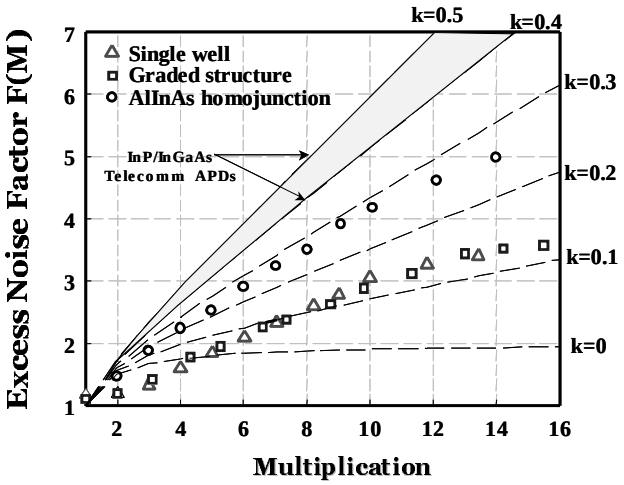

Figure 5. The measured excess noise factor F(M) curves for the single-well (triangles), pseudo-graded (squares), and homojunction 200-nm $In_{0.52}Al_{0.48}As$ (circles) APDs.

The excess noise factors, F(M), of the three structures were measured using a HP8970B noise figure meter with a standard noise source. The measurement bandwidth was 4MHz. An Argon ultra-violet laser was used to ensure pure electron injection conditions in the gain and noise measurements. Plotted in Fig. 5 are the excess noise factor curves for the three structures; theoretical curves based on local-field theory [32] are also plotted for reference purpose. Both the single-well structure and the graded-structure have an excess noise level that corresponds to an effective k [32] of ~0.1, which is well below that of the homojunction 200-nm $In_{0.52}Al_{0.48}As$ (k_{eff} ~0.2 to 0.3). It is also much lower than that of commercial InP/InGaAs APDs (k_{eff} ~0.4 to 0.5 shown as shaded region in the figure).

2.2 Large-area avalanche photodiodes

Much of the recent research on APDs has focused on achieving higher gain-bandwidth products to accommodate the ever-increasing bit rates of fiber-optic systems. For this application, small device size is preferred in order to reduce the *RC* time constant. On the other hand, emerging optical measurement systems that operate in the eye-safety wavelength range (~1.5μm) require long-wavelength, high-sensitivity photodiodes with large detection area. For many applications of this type an APD is preferable to a *p-i-n* photodiode since the internal gain of the APD affords higher sensitivity.

Similar material uniformity is required by three-dimensional infrared imaging systems, which utilize APD arrays that operate in the short wavelength infrared (SWIR) range ($0.8\mu m \leq \lambda \leq 2.2\mu m$) and have gigahertz bandwidths [33]. Both applications present stringent challenges to the quality and uniformity of the epitaxial layers from which the APDs are fabricated. In addition, passivation of the InP-based material is critical. If large defect densities are created during material growth (MBE or MOCVD), the bulk leakage

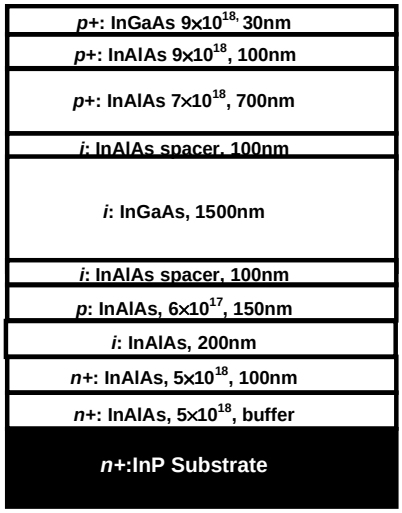

Figure 6. Device structure for large-area APDs and arrays.

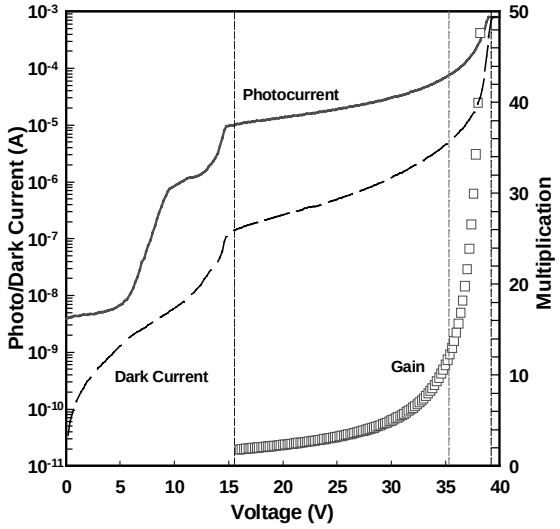

Figure 7. I-V curves for a 500μm-mesa-diameter APD.

current will be high, severe micro-plasma-induced speed degradation will result [34], and the device reliability for large-area APDs and arrays will suffer [35]. From a processing point of view, the quality of device passivation is critical if low dark currents are to be achieved [36]. In this paper, we describe $In_{0.53}Ga_{0.47}As/In_{0.52}Al_{0.48}As$ long-wavelength APDs with mesa diameter up to 500μm. The multiplied dark current density was ~2.5×10^{-2} nA/μm^2 at 90% of breakdown. An 18 × 18 APD array has also been demonstrated with the same InP-based material. This APD array exhibited uniform distributions of

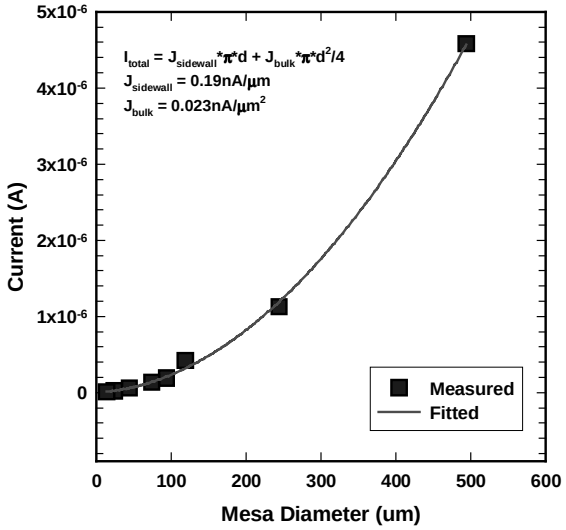

Figure 8. (a) Dark current and quadratic fit as a function of mesa diameter.

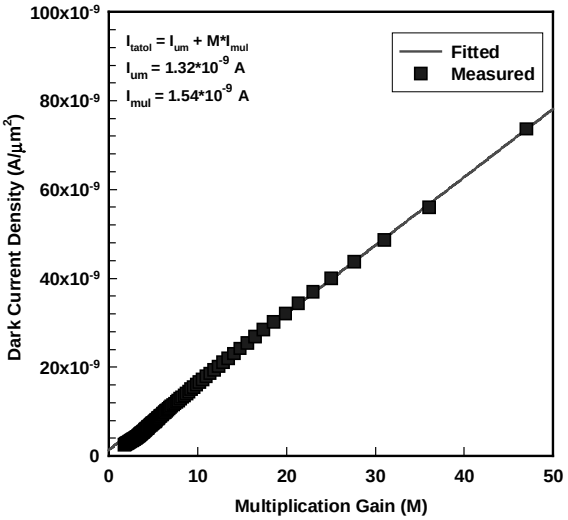

Figure 8.(b) Dark current and quadratic fit as a function of gain for a 100μm device.

breakdown voltage, dark current, and multiplication gain. The APDs in the array demonstrated bandwidth of ~8GHz at low gains and a gain-bandwidth product of ~120 GHz.

The separate absorption, charge, and multiplication (SACM) structure that was utilized for the large-area APDs and arrays is shown in Figure 6. With proper design this structure exhibits low dark current, low multiplication noise, and high speed [21,37-40]. The typical photoresponse and dark current curves of a 500μm-diameter APD are shown in Figure 7. The punch-through voltage was ~15.0V and the breakdown voltage was ~39.2V. The photocurrent was not flat above the punch-through voltage, an indication that gain has been achieved prior to punch-through [34]. In order to estimate the gain, the external quantum efficiency was measured [41] at different biases above punch-through. For bias voltage of 16.0V, the APD is clearly beyond punch-through and the external quantum efficiency was ~85% at the wavelength of 1.55μm, which is much higher than that of previous APD array devices [41], where the unity-gain external quantum efficiency was ~45% at 1.55μm. The only difference between these device structures was the charge layer doping level; the large-area APD device has ~1.85 times higher Be doping concentration in the charge layer. This APD array result can be utilized as a reliable reference for unity-gain quantum efficiency since the APD array device in Ref. [41] exhibited very flat photoresponse after punch-through and no obvious gain-enhanced quantum efficiency was observed. Based on this reference the gain at bias voltage of 16.0V can be estimated as ≥1.8. The assertion of gain at punch-through can be also corroborated by an estimate of the electric field intensity. At a reverse bias of 16.0V, the electric field in the $In_{0.52}Al_{0.48}As$ multiplication region is ~580kV/cm, assuming a 200nm $In_{0.52}Al_{0.48}As$ un-doped multiplication region and a 150nm *p*-type (6×10^{17} cm^{-3}) $In_{0.52}Al_{0.48}As$ charge region. This value of electric field is consistent with measurements on $In_{0.52}Al_{0.48}As$ homo-junction APDs [20], from which it was found that the electric field in a 200nm-thick multiplication region at gain of 1.8 was ~560KV/cm.

The dark current of a 30μm-diameter APD was ~26.7nA at bias voltage of 35.2V (90% of the breakdown where gain >10). This compares favorably with SiN_x-passivated APDs: 0.7μA/30μm by Kagawa et al [42], 0.41μA/30μm by Kim et al [35], 0.4μA/80μm by Makita et al [43], and the polyimide-passivated APDs (67nA/30μm) and the BCB-passivated APDs (38nA/30μm) reported by Kim et al [35]. The APD dark current consists of the bulk leakage current, which is proportional to the mesa area, and the sidewall leakage current, which is only proportional to the mesa perimeter. The total dark current can be expressed as:

$$I_{total} = J_{sidewall} \cdot \pi \cdot d + \frac{J_{bulk} \cdot \pi \cdot d^2}{4} \qquad (1)$$

(1)

where $J_{sidewall}$ is the sidewall leakage current density (A/m) and J_{bulk} is the bulk leakage current density (A/m^2). The measured dark currents at bias voltage of ~35.2V (90% of breakdown) are plotted in Figure 8(a) versus mesa diameter. The solid line is a quadratic fit, which shows that the bulk component of the dark current is dominant. From the fit, the surface dark current density, $J_{sidewall}$, was 0.19nA/μm and the bulk dark current density was 0.023 $nA/\mu m^2$. The total dark current can also be expressed in terms of the multiplied dark current and un-multiplied dark current using the relation:

$$I_{total} = I_{un-multiplied} + I_{multiplied} \cdot M \qquad (2)$$

In Fig. 8(b), Eq. (2) was fitted to the dark current of a 100μm-diameter APD. The un-multiplied dark current (density) was ~1.32nA (4.2pA/μm) and

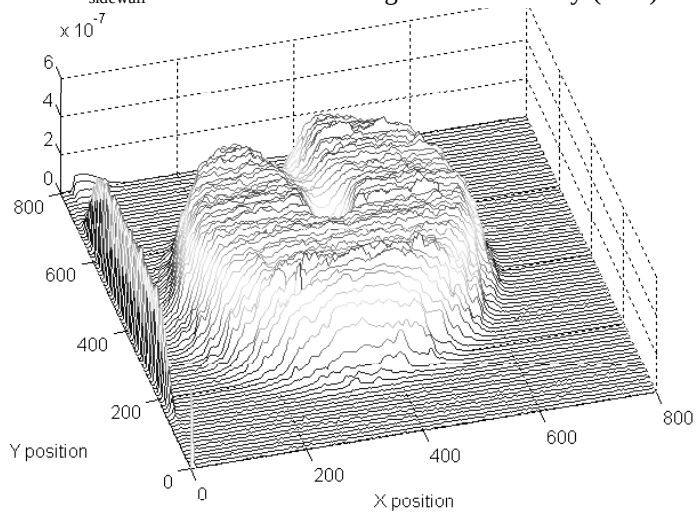

Figure 9. Spatial photo-response of a 500μm APD at bias voltage of 38.6V (*M≥20*).

the multiplied dark current was ~1.54nA. The dependence of dark current on gain remains linear to gain values > 50. The low value of the un-multiplied dark current (density) is an indication of good material quality and surface passivation; it can be neglected for APDs biased at high gains.

The spatial photoresponse profile of the large-mesa-area APD was measured by the raster-scanning technique. A 1.5-μm-wavelength He-Ne laser beam with a beam-waist <5um was scanned across a 500μm-diameter APD at bias voltage of 36.8V (M ~20). A flat, uniform photoresponse profile was obtained across the whole mesa area, as shown in Figure 9. No spikes in the interior or edge peaks were observed.

2.2 Avalanche photodiode arrays

APD arrays were also fabricated from wafers having similar structures that in Fig.6. The photocurrent, dark current, and gain of each device in an 18×18 array of 50μm-diameter APDs were measured. Three devices on the array failed due to improper probing. Statistical analysis of the dark current for the other 321 devices exhibited a mean value of ~4.4nA and a standard deviation of 1.5nA at a bias voltage of 16.0V (gain ~1.8). The dark current distribution at 90% of the breakdown voltage exhibited a mean value of ~71nA and a standard deviation of 13nA. The higher fractional spread at higher bias was due to poor sidewall passivation on several devices. Uniform photocurrent was consistently observed across the array. The mean value of gain was 10.9, 16.1, 22.1, and 43.4 at reverse bias voltages of 35.0V, 36.4V, 37.2V, and 38.2V, respectively. The standard deviations of the gain distribution at each of the above reverse bias conditions were 0.9, 1.4, 2.1, and 5.6, respectively. The bandwidth of the array devices was measured with a HP8703A lightwave component analyzer at the wavelength of 1.3μm. The low-gain bandwidth of a typical 50μm-diameter APD device was ~8GHz. The bandwidth at low gain was limited by the transit time through the long carrier transport path (~3.9μm) associated with the depleted absorption, charge, and multiplication regions. Based on measurements of the device resistance and capacitance as well as calculated values, the 3-dB *RC*-bandwidth was estimated to be >20GHz. At higher gains a gain-bandwidth product of 120GHz was observed.

3. EVANESCENTLY-COUPLED PIN PHOTODIODES

To meet the challenge of high-responsivity, broad-bandwidth and high dynamic range, many approaches have been investigated. Surface-illuminated structures such as PIN, Uni-Traveling Carrier (UTC), Dual Depletion Region (DDR) or Partially Depleted Absorber (PDA) photodiodes, have demonstrated high-power operation [44-47], however the tradeoff between quantum efficiency and transit time limits the responsivity to ≤0.6 A/W for small devices that can operate at frequencies as high as 40 GHz. Side-

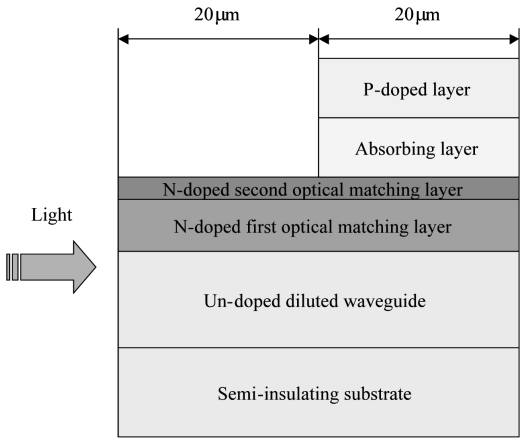

Figure 10. Schematic cross section of the Short Multimode Waveguide Photodiode.

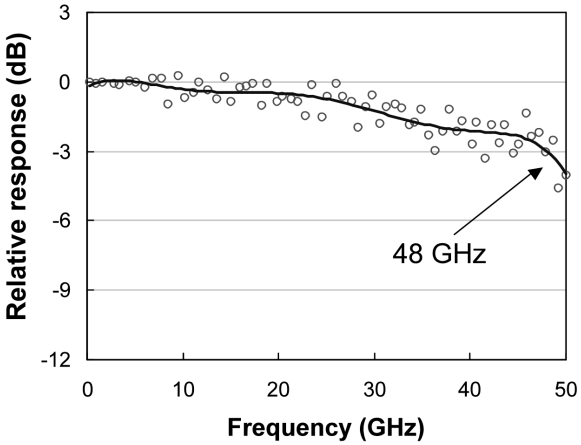

Figure 11. Frequency response of a 5×20 μm² SMWP photodiode.

illuminated photodiodes in which the responsivity and transit time are decoupled can overcome this restriction. A responsivity of 0.85 A/W and 50 GHz bandwidth have been reported [48] for edge-coupled

PINs. A primary disadvantage of this type of photodiode is poor optical power capability compared to an evanescent coupling approach [49]. Due to more uniform light absorption, devices that utilize evanescent coupling can achieve higher saturation current levels, which translates to higher dynamic range, than a side-illuminated approach [50]. Furthermore, evanescently-coupled photodiodes with an integrated taper have demonstrated responsivity up to 0.75 A/W [51] but at the expense of a more complex (and thus more difficult to fabricate) structure. We have shown that the critical taper technology can be replaced by an etched short multimode graded-index waveguide [52]. Using a Short Multimode Waveguide Photodiode (SMWP) that consists of a diluted waveguide and two optical matching layers (Fig. 10) a responsivity of 1.02 A/W and 48 GHz bandwidth were achieved.

A schematic cross section of the SMWP is shown in Fig.10. The challenge of this structure is to absorb as much light as possible over the length of a high-speed short photodiode (20-μm). The multimode waveguide consists of a diluted waveguide and two optical matching layers. The diluted waveguide is a stack of 10-periods of un-doped InP/GaInAsP (1.1-μm band gap) layers. The number of periods has been optimized to achieve high coupling efficiency with an input fiber and low TE/TM polarization dependence. The two optical matching layers are n-doped GaInAsP. The band gaps correspond to 1.1-μm and 1.4-μm for the first and second optical matching layers, respectively. This provides a gradual increase of the optical refractive index from the diluted waveguide to the absorbing layer, which results in a significant enhancement of the quantum efficiency. The epitaxial structure was grown by molecular beam epitaxy on a semi-insulating substrate. The photodiode mesas were patterned using dry etch, followed by a wet etch. The p-contact metallization was used as the etching mask and a thin InP layer on the top of the second optical matching layer served as an etch stop. A SiO_2 passivation film was then deposited. The electrical pads were isolated by etching a trench around the signal pad. An air bridge connected the photodiode and the signal pad. Finally the chips were precisely cleaved using a V-groove and an anti-reflection coating was deposited.

In agreement with the modeling, the optimal waveguide length was found to be 20-μm. 1.07 A/W responsivity was achieved at 1.543-μm wavelength (corresponding to a external quantum efficiency of 86%) with TE/TM polarization dependence less than 0.5 dB. The bandwidth and saturation current were measured with a heterodyne setup that utilizes two single mode DFB lasers were temperature-controlled and mixed in a 3 dB coupler. Figure 11 shows the bandwidth response achieved on a 5×20 μm^2 diode. A broad bandwidth of 48GHz has been measured. To our knowledge, this is the highest responsivity reported for a wide bandwidth (48 GHz) photodiode.

4. QUANTUM DOT INFRARED PHOTODETECTORS

To date, normal-incidence QDIPs with encouraging performance at ~77 K have been demonstrated from 3 μm to 14 μm wavelength. In the mid-wavelength infrared (MWIR) regime, we have previously demonstrated a peak detectivity (D*) of 1.5×10^9 $cmHz^{1/2}/W$ at 7.2 μm at 77 K in Al-free GaAs(001)/InAs n-i-n QDIPs [53,54]. To improve upon the dark current and D*, the construct of a current blocking AlGaAs layer in the otherwise GaAs confinement layers was introduced [55]. With such an AlGaAs current blocking layer, a peak D* at 6.2 μm of 10^{10} $cmHz^{1/2}/W$ at 77 K [56] was obtained. In order to shift the response to longer wavelengths, the cap layer has recently been changed from GaAs to InGaAs. Figures 12 and 13 show a schematic of the QDIP structure and the band structure, respectively. The sample was grown on semi-insulating GaAs (001) substrates by solid-source molecular beam epitaxy. Five layers of nominally 2.0 monolayer (ML) InAs at a growth rate of ~0.22 ML/sec at ~500ºC were inserted between highly Si-doped top and bottom GaAs contact layers. Then 20 ML $In_{0.15}Ga_{0.85}As$ regions were grown via migration enhanced epitaxy (MEE) at ~350ºC as the quantum dot cap layers followed by 20 ML of MEE grown GaAs. Additional 160 ML of GaAs was grown via MBE at 500º for a total of 180 ML GaAs spacer layers. The GaAs layers between the contact layers and the nearest quantum dot layer had a thickness of 220 ~ 240 MLs.

The normal-incidence spectral response of the n-i(QDs)-n QDIPs at 77K is shown in Figure 14. The intraband photoresponse peak occurred at ~8.8 μm (141 meV) for bias larger than 0.2 V. We note that the

conduction band bandoffset for the GaAs/$In_{0.15}Ga_{0.85}As$/GaAs QWs is estimated in the literature to be 145±15meV. Although this value is close to the 8.8 μm (141 meV) photoresponse, this response (more

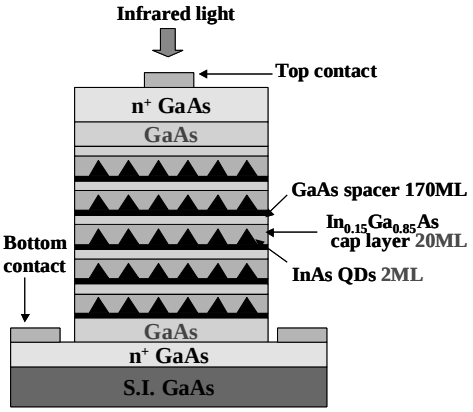

Figure 12. Schematic of an InAs/$In_{0.15}Ga_{0.85}As$/GaAs quantum dot infrared photodetector structure.

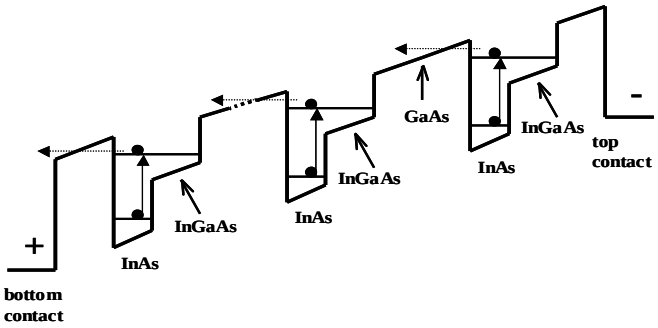

Figure 13. Schematic of the band structure an InAs/$In_{0.15}Ga_{0.85}As$/GaAs quantum dot infrared photodetector structure..

precisely, 8.22 μm at -0.8V) does not arise from the GaAs/20 ML $In_{0.15}Ga_{0.85}As$/GaAs QW regions between the InAs QD regions. This is supported by early reported experimental data [57] on infrared detector structures that contain wider GaAs/30 ML $In_{0.15}Ga_{0.85}As$/GaAs QW regions between QDs, and show a red shift (from the 8.22 micron response of the current GaAs/20ML $In_{0.15}Ga_{0.85}As$/GaAs containing sample) to 9.3 micron (at -0.8V) for the 8.8 μm photoresponse. This is in contrast to the blue shift that should result if the origin of this photoresponse peak were in the QW region between the QDs. Thus, the 8.8 μm photoresponse arises from the InAs QDs. Considering that the barrier height of $In_{0.15}Ga_{0.85}As$/GaAs is about 145 meV, the much smaller 5.4 μm (~230meV) photoresponse clearly arises from the InAs QDs. Thus, both the 8.8 μm and 5.4 μm photoresponses arise from the InAs QDs. Note that the full width half maximum (FWHM), $\Delta\lambda$, of the ~8.8 μm peak is ~1.0 μm and $\Delta\lambda/\lambda$ is ~12 %.

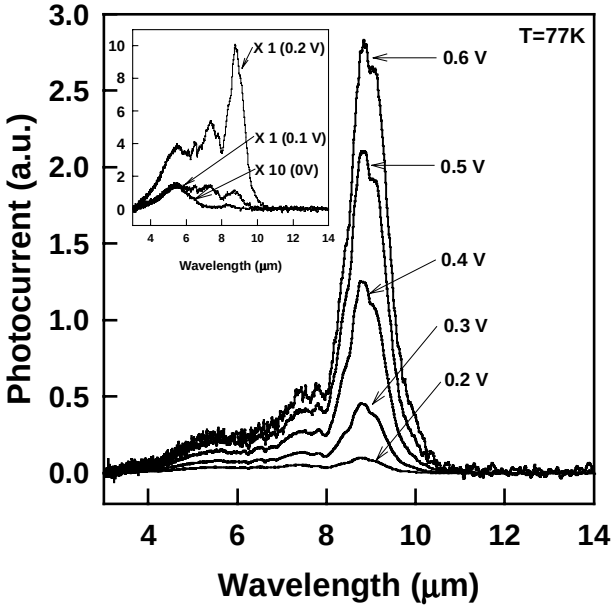

Figure 14. Normal-incidence spectral response at positive bias and 77 K measured with a FTIR spectrometer.

The absolute spectral responsivity was calibrated with a blackbody source (T = 995 K). Figure 15 shows the peak responsivity versus bias at temperatures of 77 K, 100 K, and 120 K. At 77 K, with increase in positive bias, the responsivity increased from 13 mA/W at 0.2 V to 660 mA/W at 0.9 V. For negative bias, the responsivity increased from 22 mA/W at –0.2 V to 600 mA/W at –0.9 V. The different responsivity curves for the positive and negative bias are due to the asymmetric band structure; electrons in the quantum dots experience different barrier heights depending on whether transport is toward the top or bottom contacts. Negative differential responsivity was observed with further increase in voltage, for both the positive and negative bias cases. This could be a result of "over-filling" the quantum dots, i.e., the higher dark currents that are concomitant with higher bias populate the higher states in the quantum dots and thus reduce the probability for intraband transitions. At low bias ($|V| \leq 0.1$ V),

the photocurrent increased with temperature. This is due to the fact that the electrons fill more of the ground states in the quantum dots. However, at higher bias, the photocurrent decreased with temperature, which could be a result either of "over-filling", which occurs at lower voltage with increasing temperature, or of a decrease in lifetime of photoexcited electrons due to an enhanced electron-phonon scattering.

Figure 16 shows the dark current density versus voltage characteristics for temperature in the range 20 K to 296 K. The structural asymmetry, discussed above, also resulted in asymmetric dark current density for positive and negative bias. As the temperature increased from 20 K to room temperature, the dark current

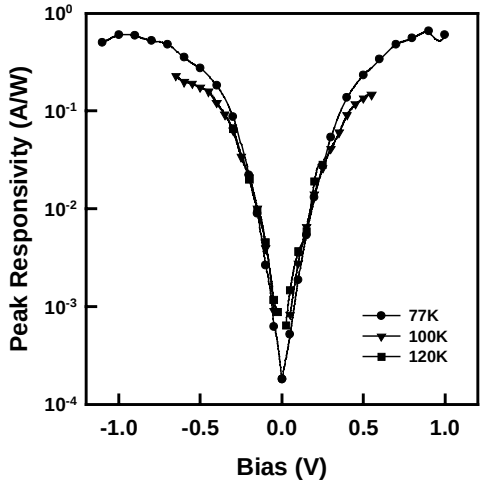

Figure 15. Absolute peak responsivities measured at 77 K, 100 K, and 120 K. The responsivities were determined using a blackbody source.

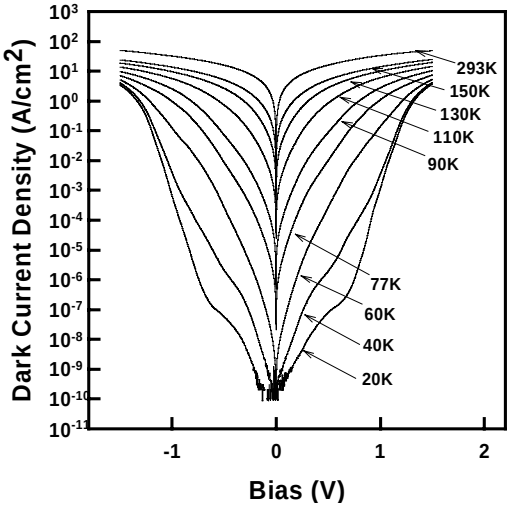

Figure 16. Dark current density vs bias curves for temperature in the range from 20 K to 293 K.

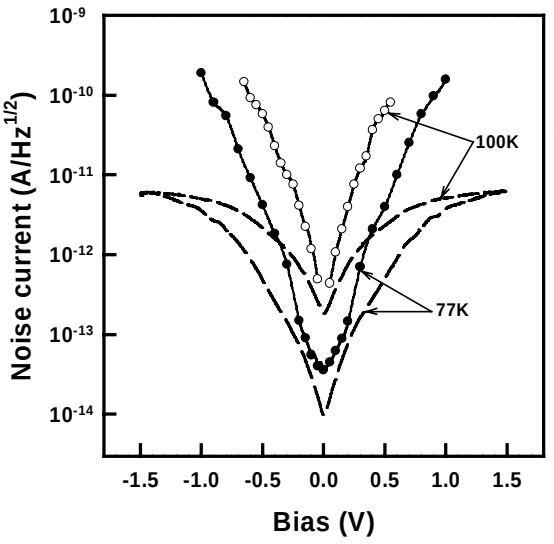

Figure 17. Measured noise current vs bias at 77 K and 100 K. The dashed lines shows calculated thermal

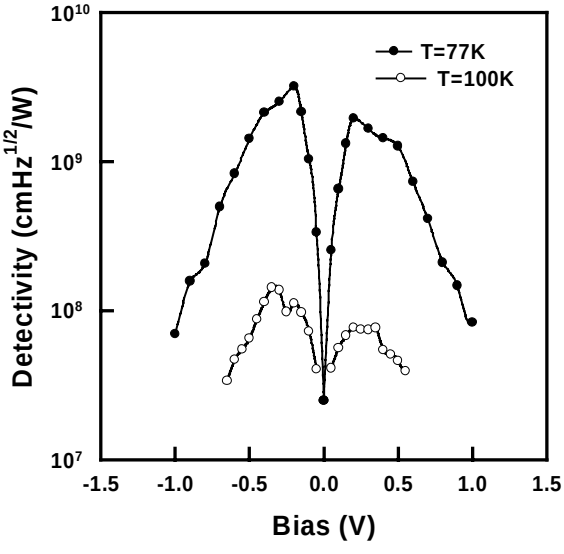

Figure 18. Peak detectivity at 77 K and 100 K.

density increased over ten orders of magnitude from 9.5×10^{-9} to 9.6 A/cm^2 at 0.3 V and from 6.2×10^{-9} to 9.6 A/cm^2 at –0.3 V. At low bias, the increase in dark current density at low temperature was due to the fact that as the bias increased, more electrons occupied the quantum dots, which resulted in an increase in the average sheet electron density. When a large fraction of the quantum dots states are occupied, further

increase in bias does not significantly alter the sheet electron density. This caused a lowering of the energy barrier for injected electrons at the contact layers, which resulted in the nearly exponential increase of the dark current.

The dark current noise current, $i_{n,}$ was characterized with low noise current preamplifiers and a SRS 760 FFT spectrum analyzer. Figure 17 shows the noise current of a 250 μm-diameter device at 77 K (solid circles) and 100 K (open circles) versus bias voltage. The calculated thermal noise current, I_{th}, at 77 K and 100 K is also shown. The thermal noise current can be expressed as, $I_{th} = (4kT/R)^{1/2}$ where k is Boltzmann's constant, T is the absolute temperature, and R is the differential resistance of the device, which was extracted from the slope of dark current. At V_B = 0.1 V and 77 K, the calculated thermal noise current (3×10^{-14} A/Hz$^{1/2}$) was close to the measured noise current (6×10^{-14} A/Hz$^{1/2}$), indicating that thermal noise is significant in the low bias region. As the bias increased, the noise current increased much faster than thermal noise. Based on the noise characteristics of quantum well infrared photodetectors, we propose that the noise current at high bias ($|V_B| > 0.1$ V) may be dominated by generation-recombination (GR) noise.

The detectivity is given by $D^* = \frac{R\sqrt{A \cdot \Delta f}}{i_n}$, where A is the device area, R is the responsivity, i_n is the noise current, and Δf is the bandwidth. Figure 18 shows the peak detectivity for the 8.3 μm and 8.8 μm peaks at 77 K and 100 K. The best performance was achieved at 77 K and –0.2 V where the peak detectivity was 3.2×10^9 cmHz$^{1/2}$/W. The corresponding responsivity was 22 mA/W. Note the rapid decrease of the detectivity with increase in temperature for both peaks. Owing primarily to the rapid increase in GR noise current at 100 K, the detectivity of the 8.3 μm peak dropped to 1.5×10^8 cmHz$^{1/2}$/W at -0.35 V.

.

5. CONCULSIONS

In conclusion, we have described recent advances in several areas of photodetector research. Impact-ionization-engineered APDs that operate at the wavelengths of interest for fiber optic applications have been demonstrated. Using either a single-well structure or a pseudo-graded structure based on InAlAs/InGaAlAs materials, low excess noise (k~0.12) was achieved. Mesa-structure $In_{0.53}Ga_{0.47}As$/ $In_{0.52}Al_{0.48}As$ avalanche photodiodes (APDs) have been utilized to fabricate large area (500μm diameter) devices and 18x18 arrays. The dark current density was ~2.5×10^{-2} nA/μm^2 at 90% of breakdown and the surface leakage current density was ~4.2pA/μm. High external quantum efficiency (53% at 0V) and high detectivity ($D^* = 2.0\times10^{14}$ cm-Hz$^{1/2}$-W^{-1} at λ = 269 nm) was achieved with solar-blind, ultra-violet $Al_xGa_{1-x}N$ photodiodes by increasing the composition of aluminum in the "window" n-layer. InAs/InGaAs/GaAs QDIPs with strain relief $In_{0.15}Ga_{0.85}As$ cap layers have been demonstrated. These QDIPs exhibited a photoresponse peak at 8.8 μm (positive bias). At 77 K, the low dark current and responsivity of 22 mA/W yielded a peak D^* of 3.2×10^9 cmHz$^{1/2}$/W.

6. ACKNOWLEDGEMENTS

This work has been supported by DARPA through the Center for Heterogeneous Integrated Photonics, the 3D Imaging Program, DARPA under N00014-99-1-0231, the Office of Naval Research under N00014-99-1-0304, and DoD Multidisciplinary University Research Initiative (MURI) program administrated by AFOSR under Grant No. F49620-98-1-0474.

REFERENCES

[1] R. D. Dupuis and J. C. Campbell, "Ultraviolet Photodetectors Based Upon III N Materials," in Wide Energy Bandgap Electronic Devices, F. Ren and J. Zolper, Eds. (World Scientific Publishing Co., Inc., 2002), to be published.

[2] J. Qu, J. Li, G. Zhang, *Solid State Communications*, 107, 467 (1998).

[3] C. J. Collins, T. Li, A. L. Beck, R. D. Dupuis, J. C. Campbell, J. C. Carrano, M. J. Schurman, and I. A. Ferguson, *Appl. Phys. Lett.*, 75, 2138 (1999).

[4] T. Kashima, R. Nakamura, M. Iwaya, H. Katoh, S. Yamaguchi, H. Amano, and I. Akasaki, *Jpn. J. Appl. Phys.*, 38, 1515 (1999).

[5] P. Schreiber, T. Dang, T. Pickenpaugh, G. Smith, P. Geherd and C. Litton, *Proc. SPIE*, 3629, 230 (1999).
[6] C. W. Litton, H. Morkoc, G. A. Smith, T. Dang, and P. J. Schreiber, to be published in *Proc. Of 46th SPIE Symp*., 4454, (2001).
[7] D. J. H. Lambert, M. .M. Wong, U. Chowdhury, C. J. Collins, T. Li, H. K. Kwon, B. S. Shelton, T.G. Zhu, J. C. Campbell and R. D. Dupuis, *Appl. Phys. Lett.*, 77, 1900 (2000).
[8] D. Walker, V. Kumar, K. Mi, P. Kung, X.H. Zhang, and M. Razeghi, *Appl. Phys. Lett*., 76, 403 (2000).
[9] J. C. Campbell, C. J. Collins, M. M. Wong, U. Chowdhury, A. L. Beck, and R. D. Dupuis, *Phys. Stat. Sol*. (a) 188, No. 1, 283– 287 (2001).
[10] G. Parish, M. Hansen, B. Morgan, S. Keller, S. P. DenBaars, U.K. Mishra, *Phys. Stat. Sol*. (a) 188, No. 1, 297– 300 (2001).
[11] E. J. Tarsa, P. Kozodoy, J. Ibbetson, B. P. Keller, G. Parish and U. Mishra, *Appl. Phys. Lett.*, 77, 316 (2000).
[12] C. J. Collins, U. Chowdhury, M. M. Wong, B. Yang, A. L. Beck, R. D. Dupuis, and J. C. Campbell, "Improved solar-blind external quantum efficiency of back-illuminated $Al_xGa_{1-x}N$ heterojunction pin photodiodes," Electron. Lett., vol. 38, pp.824-826 (2002).
[13] For a recent treatment, see S. Donati, *Photodetectors: Devices, Circuits, and Applications*, (Prentice Hall, Upper Saddle River, NJ) 2000.
[14] C. J. Collins, T. Li, D. J. H. Lambert, M. M. Wong, R. D. Dupuis, and J. C. Campbell, *Appl. Phys. Lett.*, **77**, 2810, (2000).
[15] J. C. Campbell, S. Chandrasekhar. W. T. Tsang, G. J. Qua, and B. C. Johnson, "Multiplication noise of wide-bandwidth InP/InGaAsP/InGaAs avalanche photodiodes." *J. Lightwave Technol*., vol. 7, no. 3, pp. 473-477, 1989.
[16] C. Hu, K. A. Anselm, B. G. Streetman, and J. C. Campbell, "Noise characteristics of thin multiplication region GaAs avalanche photodiodes," *Appl. Phys. Lett*., vol. 69, no. 24, pp. 3734-3736, 1996.
[17] K. F. Li, D. S. Ong, J. P. R. David, G. J. Rees, R. C. Tozer, P. N. Robson, and R. Grey, "Avalanche multiplication noise characteristics in thin GaAs p^+-i-n^+ diodes," *IEEE Trans. Electron Dev.*, vol.45, no.10, pp.2102-7, 1998.
[18] S. A. Plimmer, J. P. R. David, D. C. Herbert. T. W. Lee, G. J. Rees, P. A. Houston, R. Grey, P. N. Robson, A. W. Higgs, and D. R. Wight, "Investigation of Impact Ionization in Thin GaAs Diodes", *IEEE Trans. Electron Dev*., vol. 43, no. 7, pp. 1066-1072, 1996.
[19] K. F. Li, S. A. Plimmer, J. P. R. David, R. C. Tozer, G. J. Rees, P. N. Robson, C. C. Button, and J. C. Clark, "Low avalanche noise characteristics in thin InP p^+-i-n^+ diodes with electron initiated multiplication," *IEEE Photon. Tech. Lett.*, vol.11, pp.364-366, 1999.
[20] C. Lenox, P. Yuan, H. Nie, O. Baklenov, C. Hansing, J. C. Campbell, and B. G. Streetman, "Thin multiplication region InAlAs homojunction avalanche photodiodes," *Appl. Phys. Lett.*, vol. 73, pp. 783-784, 1998.
[21] C. Lenox, H. Nie, P. Yuan, G. Kinsey, A.L. Holmes, Jr., B.G. Streetman, J.C. Campbell, "Resonant-Cavity InGaAs/InAlAs Avalanche Photodiodes with Gain-Bandwidth-Product of 290 GHz," *IEEE Photonics Technology Letters*, vol.11, no. 9, pp. 1162-1164, 1999.
[22] P. Yuan, H. Chad, K. A. Anselm, C. Lenox, H. Nie, H. L. Holmes, B. G. Streetman, and J. C. Campbell, "Impact Ionization Characteristics of III-V Semiconductors in a Wide Range of Multiplication Region Thickness," *IEEE J. Quantum Electron.*, vol. 36, pp. 198-204, 2000.
[23] X. G. Zheng, X. Sun, S. Wang, P. Yuan, G. S. Kinsey, A.L. Holmes, Jr., B. G. Streetman, J. C. Campbell, "Multiplication Noise of $Al_xGa_{1-x}As$ Avalanche Photodiodes with High Al Concentration and Thin Multiplication Region," *Appl.Phys.Lett.*, vol.78, no.24, pp.3833-5, 2001.
[24] Chee Hing Tan, J.P.R.David, Stepen A. Plimmer, Graham J. Rees, Richard C. Tozer, and Robert Grey, "Low Multiplication Noise Thin $Al_{0.6}Ga_{0.4}As$ Avalanche Photodiodes," *IEEE Tran. Elec. Dev*., vol. 48, no.7, pp.1310-7, 2001.
[25] P. Yuan, S. Wang, X. Sun, X. G. Zheng, A.L. Holmes, Jr., and J. C. Campbell, "Avalanche Photodiodes with an Impact-Ionization-Engineered Multiplication Region," *IEEE Photonics Technology Letters*, vol. 12, no. 10, pp. 1370-72, 2000.

[26] Joe C. Campbell, Shuling Wang, X. G. Zheng, G.S. Kinsey, A. L. Holmes, Jr., X.Sun, R. Sidhu, and P. Yuan, "Ultra-Low-Noise Avalanche Photodiodes," *Proc. SPIE*, vol. 4283, pp.480-488, January 2001.

[27] S. Wang, R. Sidhu, X.G. Zheng, X. Li, X. Sun, A. L. Holmes, Jr., and J.C. Campbell, "Low-Noise Avalanche Photodiodes With Graded Impact-Ionization-Engineered Multiplication Region," *IEEE Photonics Technology Letters*, vol.13, no.12, pp.1346-8, 2001.

[28] S. Wang, F. Ma, R. Sidhu, X. G. Zheng, X. Sun, A. L. Holmes, Jr., and J. C. Campbell, "Ultra-low noise avalanche photodiodes with a 'centered-well' multiplication region," to be published.

[29] F. Ma, S. Wang, X. Li, K.A. Anselm, X.G. Zheng, A. L. Holmes, Jr., and J. C. Campbell, "A Monte Carlo Simulation of Low-Noise Avalanche Photodiodes with Heterojunctions," Accepted for publication in *J. Appl. Phys.,* 2002.

[30] M. Tsuji, K. Makita, I. Watanabe and K. Taguchi, "High-crystallinity MOVPE-grown sawtooth-bandgap $In_{1-x-y}Ga_xAl_yAs$ for use in staircase avalanche photodiodes," *J. Crystal Growth*, vol. 180, pp. 9-14, 1997.

[31] Y. Okuto and C. R. Crowell, "Ionization coefficients in semiconductors: A nonlocal property," *Phys. Rev. B*, vol. 10, pp. 4284-4296, 1974.

[32] R.J. McIntyre, "Multiplication noise in uniform avalanche diodes," *IEEE Trans. on Electron Dev.*, vol. 13, no. 1, pp. 164-168, 1966.

[33] R. S. Balcerak, "3D imaging", 3D imaging Receivers SPIE Conference, April, 2000

[34] G. S. Kinsey, J. C. Campbell, and A. G. Dentai, "Waveguide avalanche photodiode with a gain-bandwidth product of 320 GHz", *IEEE Photonics Technology Letters*, Vol. 13, Issue 8, 842-844, August 2001

[35] H.S. Kim, J.H. Choi, H.M. Bang, Y. Jee, S.W. Yun, J. Burm, M.D. Kim, and A.G. Choo, "Dark current reduction in APD with BCB passivation", *Electronics Letters*, pp 455-457, *29,*Vol. 37, no. 7, March 2001

[36] D. Schmidt and D. Trommer, "Conservation of low dark current of InGaAs photodiodes after NH_3F/HF etch a BCB passivation layer", Indium Phosphide and Related Materials, 2000 Conference Proceedings, Page 302 -305

[37] K. Makita, I. Watanabe, M. Tsuji, K. Taguchi, "150 GHz GB-Product and Low dark Current InAlGaAs Quaternary Well Superlattice Avalanche Photodiodes," Proc. IOOC-95,1995

[38] Cohen-Jonathan, C., Giraudet, L., Bonzo, A., and Praseuth, J. P.: 'Waveguide AlInAs/GaAlInAs avalanche photodiode with a gain-bandwidth product over 160GHz', *Electron. Lett.*, 1997, vol. 33, no. 17, pp.1492-1493

[39] Nie, H., Anselm, K. A., Lenox, C., Yuan, P., Hu, C., Kinsey, G., Streetman, B. G., and Campbell, J. C. "Resonant-cavity separate absorption, charge, and multiplication avalanche photodiodes with high speed and high gain-bandwidth product," *IEEE Photon. Technol. Lett*., 1998, vol. 10, no. 3, pp. 409-411

[40] K. Kato, "Ultrawide-Band/High-frequency Photodetectors," *IEEE Trans. on Microwave Theory and Techniques*, Vol. 47, no. 7, 1265-1281, July 1999

[41] X. G. Zheng, J. Hsu, X. Sun, J. B. Hurst, X. Li, S. Wang,, A.L. Holmes, Jr., J. C. Campbell, A. S. Huntington, L. A. Coldren, "A 12×12 $In_{0.53}Ga_{0.47}As/In_{0.52}Al_{0.48}As$ Avalanche Photodiode Array", to be published.

[42] Kagawa, T., Kawamura, Y., and Iwamura, H., 'A wide-bandwidth low-noise InGaAsP-InAlAs superlattice avalanche photodiode with a flip-chip structure for wavelength of 1.3μm and 1.55μm', *IEEE J. Quantum Electron.*, 1993, 29, pp 1387-1392

[43] Makita, K., Watanabe, I., Tsuji, M., and Taguchi, K., "Dark current and breakdown analysis in In(Al)GaAs/InAlAs superlattice avalanche photodiodes", *Jpn. J. Appl. Phys.*, 1996, 35, pp. 3440-3444.

[44] K. J. William and R.D. Esman, "Large-signal compression-current measurements in high-power microwave pin photodiode," IEEE Photonics tech. lett., vol.35, 82-83 (1999).

[45] N. Shimizu, N. Watanabe, T. Furuta, T. Ishibashi, "InP-InGaAs Uni-Traveling-Carrier Photodiode with Improved 3-dB Bandwidth of Over 150GHz", IEEE Photonics Tech. Lett., Vol. 10, 412-414 (1998).

[46] F. J. Effenberger and A. M. Joshi, "Ultrafast, Dual-Depletion Region InGaAs/InP pin Detector", IEEE J. Lightwave Tech., Vol. 14, 1859-1864 (1996).

[47] X. Li, N. Li, X. Zheng, S. Demiguel, J. Campbell, D. Tulchinsky, K. Williams, "High-speed High-saturation-current InP/$InGa_{0.53}As_{0.47}$ Photodiode with partially depleted absorber", in proc. OFC'03, paper WF3.
[48] K. Kato, S. Hata, K. Kawano, J. - I. Yoshida, and A. Kozen, "A High - Efficiency 50 GHz InGaAs Multimode Waveguide Photodetector," IEEE J. Quantum Electron., vol. 28, 2728-2735, (1992).
[49] G. Unterbörsh, D. Trommer, A. Umbach, R. Ludwig, and H. G. Bach, "High-power performance of a high-speed photodetector," in Proc. ECOC'98, pp. 67-68.
[50] S. Demiguel, L. Giraudet, L. Joulaud, J. Decobert, F. Blache, V. Coupé, F. Jorge, P. Pagnod-Rossiaux, E. Boucherez, M. Achouche, and F. Devaux, "Evanescently Coupled Photodiodes Integrating a Double Stage Taper for 40 Gb/s Applications – Compared Performance with Side-Illuminated Photodiodes," IEEE J. Lightwave Tech., Vol. 12, 2004-2014 (2002).
[51] F. Xia, J. K. Thomson, M.R. Gokhale, P.V. Studenkov, J. Wei, W. Lin and S.R. Forrest, "An Asymmetric Twin-Waveguide High-Bandwidth Photodiode Using a Lateral Taper Coupler", IEEE Photonics Tech. Lett., Vol. 13, 845-847 (2001).
[52] Stephane Demiguel, Ning Li, Xiaowei Li, Xiaoguang Zheng, Jooyong Kim, Joe C. Campbell, Hanfei Lu, and Alex Anselm, "Very high-responsivity evanescently-coupled photodiodes integrating a short multimode waveguide for high-speed applications", to be published.
[53] Z.H. Chen, O. Baklenov, E. T. Kim, I. Mukhametzhanov, J. Tie, A. Madhukar, Z.M. Ye and J. C. Campbell, J. Appl. Phys. 89, 4558 (2001)
[54] Z. M. Ye and J. C. Campbell, Z. H. Chen, E. T. Kim, and A. Madhukar, submitted to Appl. Phys. Lett.; Z.M. Ye, J. C. Campbell, Z.H. Chen, O. Baklenov, E. T. Kim, I. Mukhametzhanov, J. Tie, and A. Madhukar, *Mat. Res. Soc. Symp. Proc.* Vol. 692, H9.17.1, (2002)
[55] O. Baklenov, Z.H. Chen, E.T. Kim, I. Mukhametzhanov, A. Madhukar, F. Ma, Z. Ye, B. Yang, and J. Campbell, the 58th IEEE Device Research Conference, (Denver, Colorado, June 19-21, 2000), p171; Z.H. Chen, O. Baklenov, E.T. Kim, I. Mukhametzhanov, J. Tie, A. Madhukar, Z. Ye, and J. Campbell, *Proceedings of QWIP2000 Workshop*, Dana Point, CA, July 2000, Infrared Physics & Technology, 42, 479 (2001)
[56] Zhengmao Ye, J. C. Campbell, Z. Chen, E.-T. Chen, and A. Madhukar, "Normal-incidence InAs self-assembled quantum-dot infrared photodetectors with high detectivity," *IEEE J. Quantum Electron.*, vol. 38, pp. 1234-1237 (2002).
[57] V. Ryzhii, *Sci. Technol.* 11, 759 (1996)